Preliminary Calculated Scatter from Trihedral Corner Reflector with WIPL-D

Eric L. Mokole
Naval Research Laboratory
Washington, DC 20375, USA
mokole@radar.nrl.navy.mil

Brian T. Gold
Naval Research Laboratory
Washington, DC 20375, USA
bgold@cmu.edu

Tapan K. Sarkar
Syracuse University
Syracuse, NY 13244, USA
tksarkar@syr.edu

Abstract: WIPL-D is being used to compute monostatic and bistatic radar cross sections of a trihedral corner reflector over the frequency range of 1-12 GHz. Initial results are discussed for vertically and horizontally polarized fields at two frequencies (1.5 and 3.8 GHz). These computations are being used to provide a benchmark against which the performance of WIPL-DP, a parallelized version of the WIPL-D, may be compared. Recently, sea-scatter data was collected from 1.9-11.5 GHz with trihedral reflectors. Since the WIPL-D calculations discussed here, as well as planned calculations, will be used to provide predictions of sea scatter that will be compared to the actual data, the sea-scatter geometry is described.

Keywords: Trihedral, Radar Cross Section, Monostatic, Bistatic, WIPL-D, CHSSI

1. Introduction

Monostatic and bistatic radar cross sections of a trihedral corner reflector are calculated with the WIPL-D electromagnetics code at two frequencies (1.5 GHz and 3.8 GHz) for vertically and horizontally polarized fields to provide a benchmark against which WIPL-DP, a parallelized version of the WIPL-D [1], may be compared. WIPL-DP is currently being developed under the sponsorship of the DoD's High Performance Computer Modernization Office (HPCMO – http://www.hpcmo.hpc.mil/) in one of its Common HPC Software Support Initiatives (CHSSIs), entitled Parallel Scene Generation/Electromagnetic Modeling of Complex Targets in Complex Clutter and Propagation Environments. This CHSSI is a joint university-industry-government effort led by the Air Force Research Laboratory and Black River Systems Corp. The motivation behind the trihedral analysis is to provide one of two sufficiently difficult, but pertinent and numerically accessible, Navy applications to test the capability of WIPL-DP. The relevant Navy problem associated with the trihedral is to understand the target-like artifacts in radar returns called sea spikes that are induced by ocean scatter [2].

Historically, the trihedral corner reflector has been used for instrumentation purposes, radar calibration, and devices with enhanced radar cross section (RCS) [3-5]. Until recently, most scattering studies of the trihedral have been understood through optics and empirical evidence, as a result of the excessively large computational burden imposed by this problem. With advances in simulation tools and computational capabilities, the trihedral corner reflector is revisited.

Trihedral corner reflectors have recently been used in a series of ultrawideband (UWB) measurements at the Atlantic Underwater Test and Experiment Center (AUTEC) in the Bahamas to investigate the low-elevation (grazing angles less than 4°) scatter of RF signals from the open ocean in an attempt to understand and mitigate the phenomenon known as sea spikes [6]. Sea spikes introduce undesirable, false, target-like artifacts in the received signals of ship-based radars – a very serious impediment to detecting real targets. A state-of-the-art, UWB, ultra-high resolution, dual-polarized radar, designed and built by Pete Hansen of the Radar Division of the Naval Research Laboratory, has been taking these short-pulse UWB measurements at S-band and X-band.

The AUTEC geometry (Fig.1) has a 1-m, anodized-aluminum, right-trihedral reflector mounted on a tower that is 8.1 m above the sea surface and 242 m from the shore-mounted UWB radar, called the microwave microscope (MWM). The transmitted signal travels on four paths before it returns to the receive antenna: (1) the direct path between the MWM and the trihedral; (2) the one-bounce path from transmitter to ocean to trihedral to receiver; (3) the one-bounce path from transmitter to trihedral to ocean to receiver; and (4) the double-bounce path from transmitter to ocean to trihedral to ocean to receiver. For this work, the sea surface is assumed to be a perfectly conducting flat plate, so that one need only consider the specular reflections corresponding to these four paths. Paths (1) and (4) are monostatic from the target's perspective, while paths (2) and (3) are bistatic

Report Documentation Page

Form Approved
OMB No. 0704-0188

1. REPORT DATE	2. REPORT TYPE	3. DATES COVERED
23 APR 2004	**N/A**	**-**

4. TITLE AND SUBTITLE	5a. CONTRACT NUMBER
Preliminary Calculated Scatter from Trihedral Corner Reflector with WIPL-D	5b. GRANT NUMBER
	5c. PROGRAM ELEMENT NUMBER
6. AUTHOR(S)	5d. PROJECT NUMBER
	5e. TASK NUMBER
	5f. WORK UNIT NUMBER
7. PERFORMING ORGANIZATION NAME(S) AND ADDRESS(ES) **Naval Research Laboratory Naval Research Laboratory Washington, DC 20375, USA**	8. PERFORMING ORGANIZATION REPORT NUMBER
9. SPONSORING/MONITORING AGENCY NAME(S) AND ADDRESS(ES)	10. SPONSOR/MONITOR'S ACRONYM(S)
	11. SPONSOR/MONITOR'S REPORT NUMBER(S)

12. DISTRIBUTION/AVAILABILITY STATEMENT
Approved for public release, distribution unlimited

13. SUPPLEMENTARY NOTES
See also ADM001763, Annual Review of Progress in Applied Computational Electromagnetics (20th) Held in Syracuse, NY on 19-23 April 2004., The original document contains color images.

14. ABSTRACT

15. SUBJECT TERMS

16. SECURITY CLASSIFICATION OF:			17. LIMITATION OF ABSTRACT	18. NUMBER OF PAGES	19a. NAME OF RESPONSIBLE PERSON
a. REPORT	b. ABSTRACT	c. THIS PAGE			
unclassified	**unclassified**	**unclassified**	**UU**	**10**	

relative to the target. Conventional optical analysis has only been applied to the monostatic radar cross section (RCS), and most bistatic RCS has been obtained by experiment. By leveraging the computational capabilities of modern workstations, monostatic and bistatic radar cross sections (RCSs) of the trihedral reflector are simulated.

The MWM generates an UWB short-pulse signal by impulse exciting a TWT. Three TWTs are used to cover the frequency bands: 1-2 GHz; 1.9-5.5 GHz; 6.5-11.5 GHz. The nominal center frequencies and range resolutions corresponding to these bands respectively are (1.5 GHz, 15 cm), (3.8 GHz, 3 cm), and (9 GHz, 2 cm). Although calculations are being made for each frequency band, only calculations at 1.5 GHz and one calculation at 3.8 GHz were available when preparing this paper.

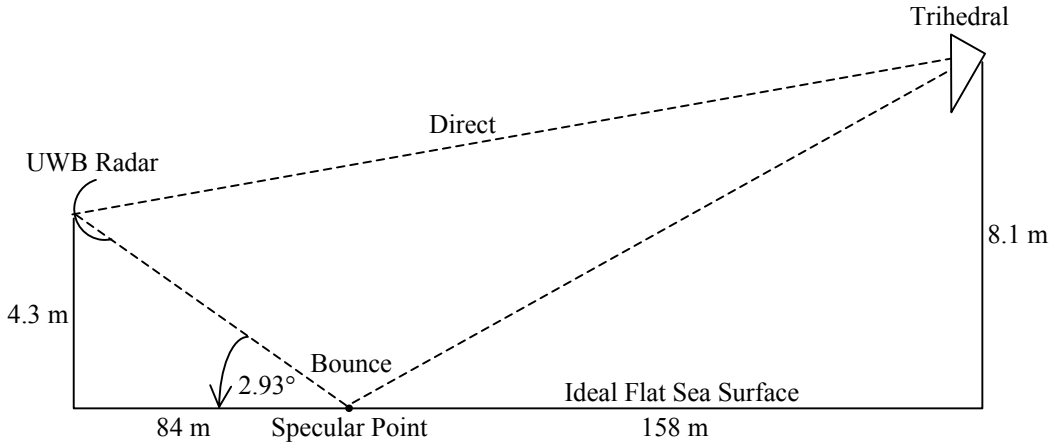

Fig.1. AUTEC experimental geometry (not to scale), with 2.93° grazing angle.

2. Trihedral and WIPL-D Geometries

The trihedral is composed of three right isosceles triangles ($\Delta n_1n_3n_8$, $\Delta n_1n_2n_3$, and $\Delta n_1n_8n_2$ in Fig. 2), where Fig. 2 shows the screen capture of the WIPL-D interface, the largest edges (n_2n_3, n_3n_8, n_8n_2) have length a (which is 1 m in the ensuing calculations), $\{n_i\}$ are the trihedral grid points from WIPL-D, and $P(n_i)$ is the coordinate of n_i. WIPL-D and WIPL-DP model plate structures with quadrilateral surfaces and impose the restriction that the quadrilaterals be convex. Therefore, each triangular side is modeled using three smaller plates. To ease the geometric-modeling complexity, the three shared edges (n_1n_2, n_1n_3, and n_1n_8) between adjacent triangular sides are aligned respectively with the Cartesian axes x, y, and z, where the origin is placed at vertex n_1 of the trihedral. Spherical angles in the WIPL-D codes are measured from the x-axis towards the y-axis (azimuth or longitude ϕ) and from the xy-plane towards the z-axis (elevation or latitude θ), which is $90° - \vartheta$, where the co-latitude ϑ is the usual spherical angle. In Fig. 2, one is looking into the trihedral along the axis of symmetry through vertex n_1. In 3-dimensional space, n_1 lies behind the plane of triangle $\Delta n_1n_2n_8$, and the axis of symmetry is perpendicular to this plane.

All three triangles that comprise the trihedral are congruent and, consequently, have the same dimensions. In particular, from a planar view of triangle $\Delta n_1n_2n_3$ (Fig. 3), one can see that edge n_2n_3 determines the dimensions of $\Delta n_1n_2n_3$, edges n_1n_2 and n_1n_3 have length $0.707a$, point n_4 is the centroid of $\Delta n_1n_2n_3$, and points n_5, n_6, and n_7 are the midpoints of their respective edges.

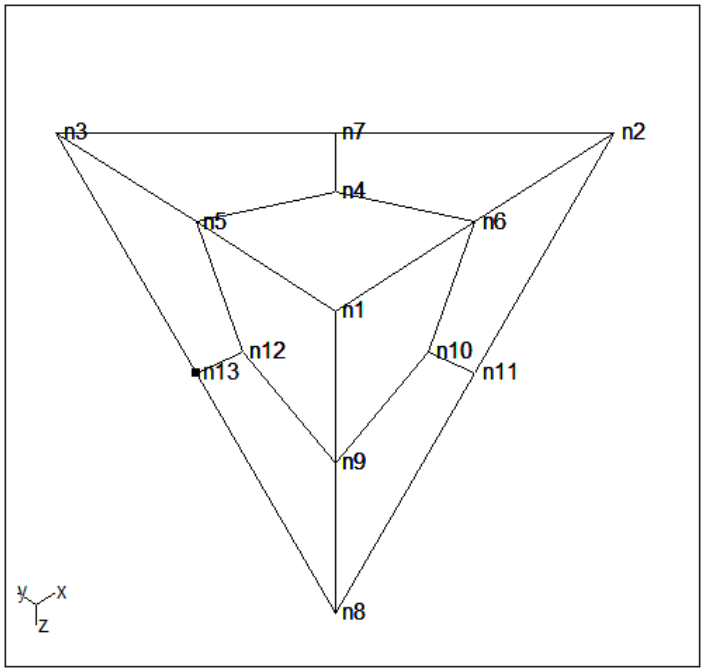

$$P(\mathrm{n}_1) = (0,0,0)$$
$$P(\mathrm{n}_2) = (a/\sqrt{2},0,0)$$
$$P(\mathrm{n}_3) = (0,a/\sqrt{2},0)$$
$$P(\mathrm{n}_4) = (a/(3\sqrt{2}),a/(3\sqrt{2}),0)$$
$$P(\mathrm{n}_5) = (0,a/(2\sqrt{2}),0)$$
$$P(\mathrm{n}_6) = (a/(2\sqrt{2}),0,0)$$
$$P(\mathrm{n}_7) = (a/(2\sqrt{2}),a/(2\sqrt{2}),0)$$
$$P(\mathrm{n}_8) = (0,0,a/\sqrt{2})$$
$$P(\mathrm{n}_9) = (0,0,a/(2\sqrt{2}))$$
$$P(\mathrm{n}_{10}) = (a/(3\sqrt{2}),0,a/(3\sqrt{2}))$$
$$P(\mathrm{n}_{11}) = (a/(2\sqrt{2}),0,a/(2\sqrt{2}))$$
$$P(\mathrm{n}_{12}) = (0,a/(3\sqrt{2}),a/(3\sqrt{2}))$$
$$P(\mathrm{n}_{13}) = (0,a/(2\sqrt{2}),a/(2\sqrt{2}))$$

Fig. 2. Frontal view of a right trihedral corner reflector along the axis of symmetry through vertex n_1, with the complete WIPL-D node geometry and scatterer coordinate system. The positive *x*, *y*, and *z* axes coincide with line segments $\mathrm{n}_1\mathrm{n}_2$, $\mathrm{n}_1\mathrm{n}_3$, and $\mathrm{n}_1\mathrm{n}_8$, respectively, and $P(\mathrm{n}_i)$ is the coordinate of n_i.

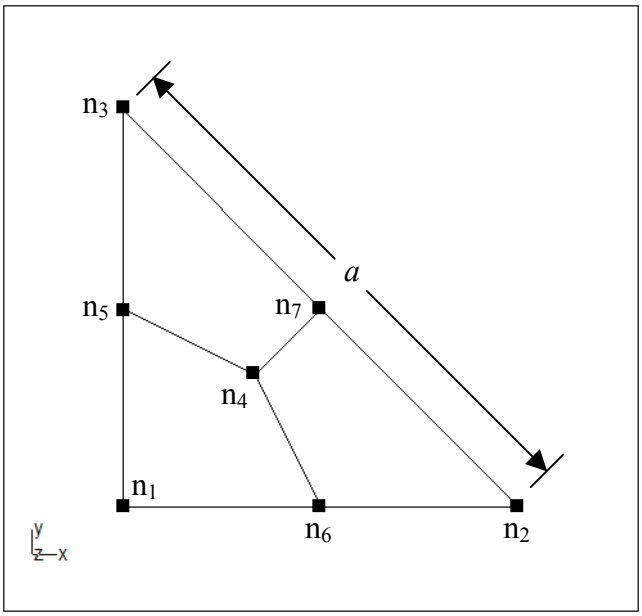

Fig. 3. Geometry of the single triangular side $\Delta\mathrm{n}_1\mathrm{n}_2\mathrm{n}_3$ comprising the trihedral, where $P(\mathrm{n}_i)$ is the coordinate of n_i, the positive *x* and *y* axes respectively coincide with line segments $\mathrm{n}_1\mathrm{n}_2$ and $\mathrm{n}_1\mathrm{n}_3$, and the positive *z* axis points out of the paper.

To relate the AUTEC and WIPL-D geometries, consider the side view of the trihedral (Fig. 4) relative to the AUTEC geometry (Fig. 1). In this configuration, θ_f is the angle from the *xy*-plane to a horizontal plane ($\theta = \theta_f$) parallel to the ideal sea surface. Note that this plane includes the trihedral's axis of symmetry ($\phi = 45°$, $\theta = \theta_f = 35.26°$). The angles β and α are specific to the AUTEC configuration, where β is the angle between the symmetry axis and the radar-trihedral line of sight ($\phi = 45°$, $\theta = \theta_f + \beta$) and α is the angle between the radar-trihedral line of sight and the specular point on the sea surface ($\phi = 45°$, $\theta = \theta_f + \beta + \alpha$). From trigonometry, $\alpha = 2.03°$, $\beta = 0.90°$, and the grazing angle is $\alpha + \beta = 2.93°$.

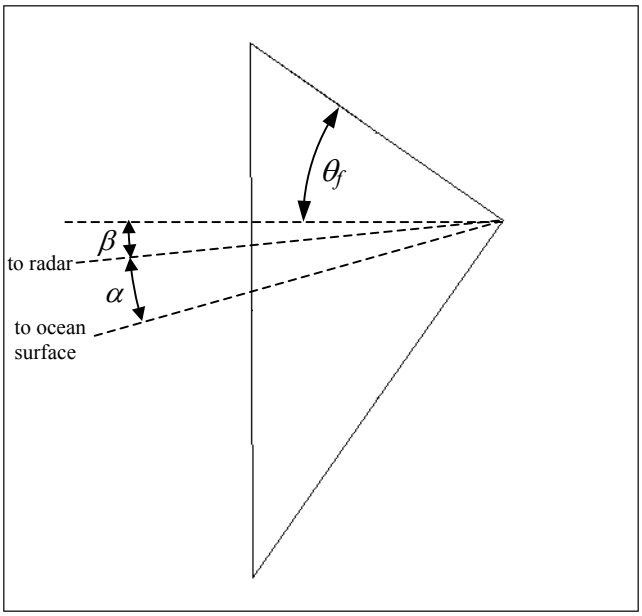

Fig. 4. Side view of trihedral showing angles relevant to AUTEC experiments.

3. WIPL-D Experiments

Two basic classes of numerical experiments have been performed: monostatic RCSs at 1.5 GHz and 3.8 GHz; and bistatic RCSs at 1.5 GHz at specific incidence and arbitrary observation angles. These two classes are studied in anticipation of numerical experiments that are specific to collected data with the AUTEC geometry and future RCS measurements of trihedrals in a compact range. Since the AUTEC data has been collected at horizontal and vertical polarizations from 1-11.5 GHz, five frequencies of interest for numerical simulation are listed in Table 1, with the associated WIPL-D modeling requirements for a 1-m corner reflector.

Despite its simple geometric structure, the trihedral corner reflector is a complex target for computational-electromagnetics solvers. As the frequency and target size *a* increase, the number of unknowns required by WIPL-D grows exponentially. This scaling in computational requirements quickly poses problems, even for modern workstations, and indicates that the trihedral corner reflector is an excellent benchmark for computational solvers. The storage requirements are independent of the computer used; however, solution times will vary with computer. The results shown here are computed on a Pentium-4, 2.5-GHz workstation with 1 GB of RAM and 512 kB of L2 cache. Unfortunately, the storage required to simulate the 7-11 GHz range is beyond the capability of any 32-bit workstation. Thus, to collect data at these higher frequencies, a more sophisticated computer must be used – for example, a parallel computer or 64-bit workstation. Consequently, only data at 1.5 and 3.8 GHz can be shown at this time.

Frequency	a/λ	Number of Unknowns (u)	Storage Required ($8u^2$)
1.5 GHz	5.00	960	7.2 MB
3.8 GHz	12.67	5131	200 MB
7.0 GHz	23.33	13955	1.5 GB
9.0 GHz	30.00	25702	5.1 GB
11.0 GHz	36.67	35833	9.8 GB

Table 1. WIPL-D modeling requirements for various frequencies.

3.1. Monostatic RCS

With the trihedral aligned along the *x*, *y*, and *z* axes, the trihedral acts as a corner in the octant containing positive *x*, *y*, and *z* components, which corresponds to $0° < \phi < 90°$ and $0° < \theta < 90°$. While most of the interesting scattering occurs in this octant (the optical field of view of the trihedral), some scattering does occur in the other seven octants. In Fig. 5, three scattering zones are apparent in the resulting 3-dimensional RCS patterns of the vertically polarized field (horizontal and vertical refer to the θ-component and the ϕ-component of the field, respectively). This pattern is obtained by mapping the nonnegative RCS value as the distance from origin n_1 in the (ϕ,θ) direction. The strong region in the middle of the pattern occurs when incident waves are reflected off all three triangular faces – hence this area is termed the *triple-bounce* zone. Similar scattering regions occur when waves bounce off two sides (*double bounce*) and one side (*single bounce*). The peak RCSs are seen in the triple-bounce zone, which is the dark hexagonal region centered about the trihedral axis of symmetry. Beyond the hexagonal region, the RCS drops off quickly, until it significantly increases for directions that are nearly parallel to the trihedral boundaries. The triple-bounce, hexagonal region is called the effective aperture [5].

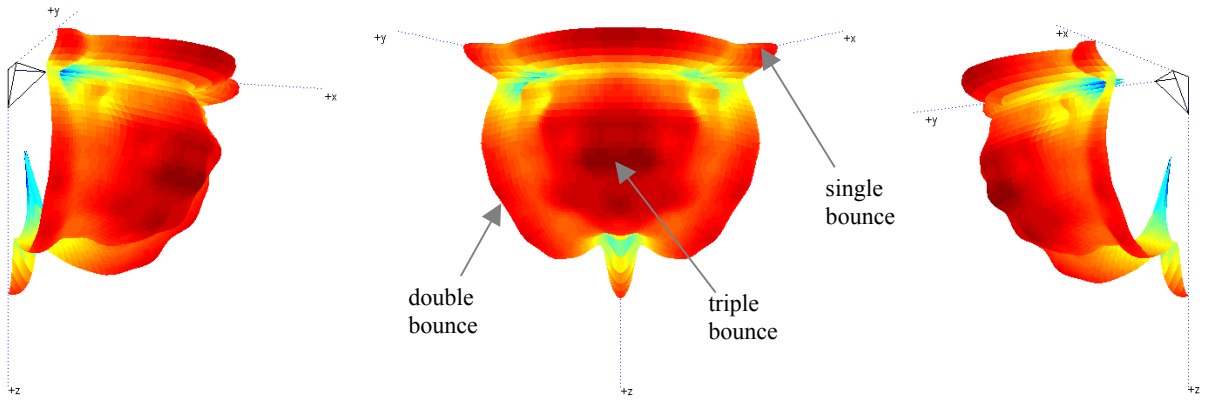

Fig. 5. Three views of the 3-dimensional vertically polarized monostatic RCS for a 1-m trihedral at 1.5 GHz within the optical field of view of the positive *xyz* octant, where the data are normalized relative to λ^2 and the dark and light shading denote large and small RCS, respectively.

The monostatic RCS at 1.5 GHz is plotted in Fig. 6 for two perpendicular planes that intersect the surface in Fig. 5: (a) $\phi = 45°$ and $0° < \theta < 90°$; and (b) $\theta = 35.26°$ and $0° < \phi < 90°$. In Fig. 6b, the vertical and horizontal

polarizations are symmetric about $\phi = 45°$, as expected from the geometry, and decrease slowly as ϕ moves away from 45° for $25° < \phi < 75°$, where they differ by less than 2 dBsm. Near $\phi = 12°$ and 78°, the horizontal RCS drops significantly (more than 5 dBsm). As ϕ approaches 0° and 90°, both polarizations increase to a significant fraction of the peak values attained along the axis of symmetry ($\phi = 45°, \theta = 35.26°$), because significant backscatter is produced by triangles $\Delta n_1 n_8 n_2$ and $\Delta n_1 n_3 n_8$, respectively.

For case (a), where the plane symmetrically bisects the trihedral, the RCSs for both polarizations behave asymmetrically as θ varies from 0° and 90° (Fig. 6a), that is, as θ varies from direction $n_1 n_7$ to direction $n_1 n_8$. Again the polarizations tend to track each other to within 3-5 dBsm. In addition, both polarizations have significantly lower RCSs near $\theta = 74°$, where very little energy (approximately 1/100) is reflected. When the plots in Fig. 6 are visually compared to results in the literature [4,5,7-9], the curves have the same general shape, with the curves in Fig. 6 having more ripple than those predicted by optical theory [7-9], because WIPL-D includes the effects of diffraction. For example, in Figs. 9 and 10 of Ref. [8], except for differences in magnitude of the local minima and the location of one null, the RCSs for horizontal polarization appear to be smoother versions of Figs. 6a and 6b, respectively, for comparable a/λ (4.99).

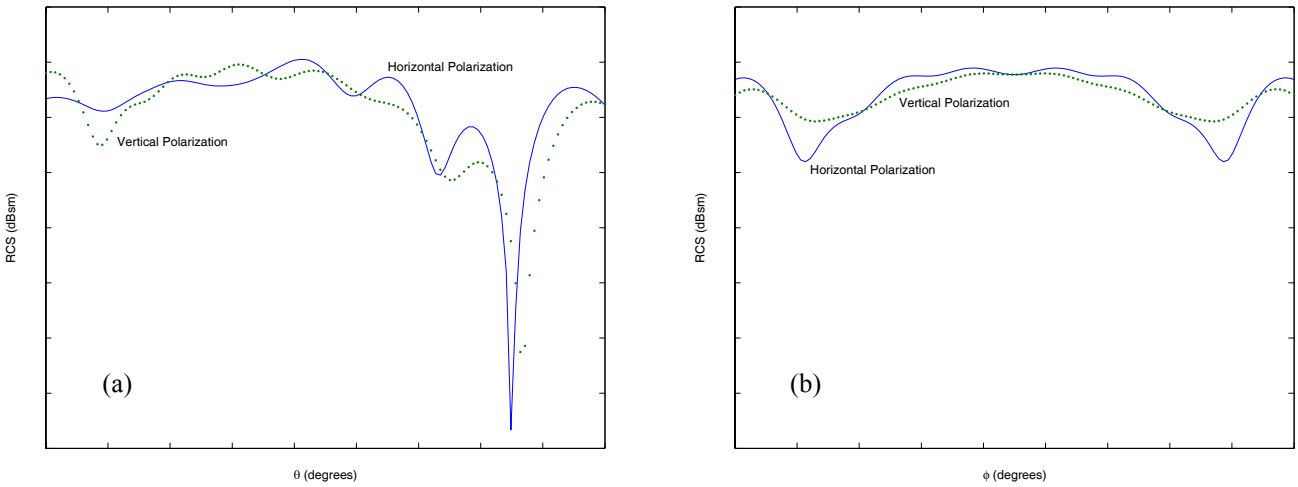

Fig. 6. Monostatic RCS of trihedral at 1.5 GHz for vertically polarized (dotted curves) and horizontally polarized (solid curves) incident fields calculated with WIPL-D: (a) $\phi = 45°$ and $0° < \theta < 90°$; (b) $\theta = 35.26°$ and $0° < \phi < 90°$.

In Fig.7, the monostatic RCSs are displayed for 1.5 GHz and 3.8 GHz as 2-dimensional projections of the 3-dimensional surface mappings (like Fig. 5) onto the plane that is perpendicular to the trihedral axis of symmetry. The positive octant ($0° < \phi < 90°$ and $0° < \theta < 90°$) is mapped onto the equilateral curved triangles of Fig. 7, where white and black of the gray-scale bar indicate high (20 dBsm) and low (0 dBsm) RCSs, respectively. On close scrutiny of the 1.5-GHz plots, one can discern the hexagonal region associated with the effective aperture (triple-bounce region) that returns the greatest energy in the optical approach and the low RCS returns from directions near, but not equal to, the Cartesian axes (x,y,z). Moreover, the horizontal and vertical RCSs at 1.5 GHz have noticeable differences, for example, the location and depth of the nulls. In contrast, at 3.8 GHz, the effective aperture is considerably bigger, with slightly larger RCSs for the horizontally polarized fields, and the difference between polarizations is less obvious.

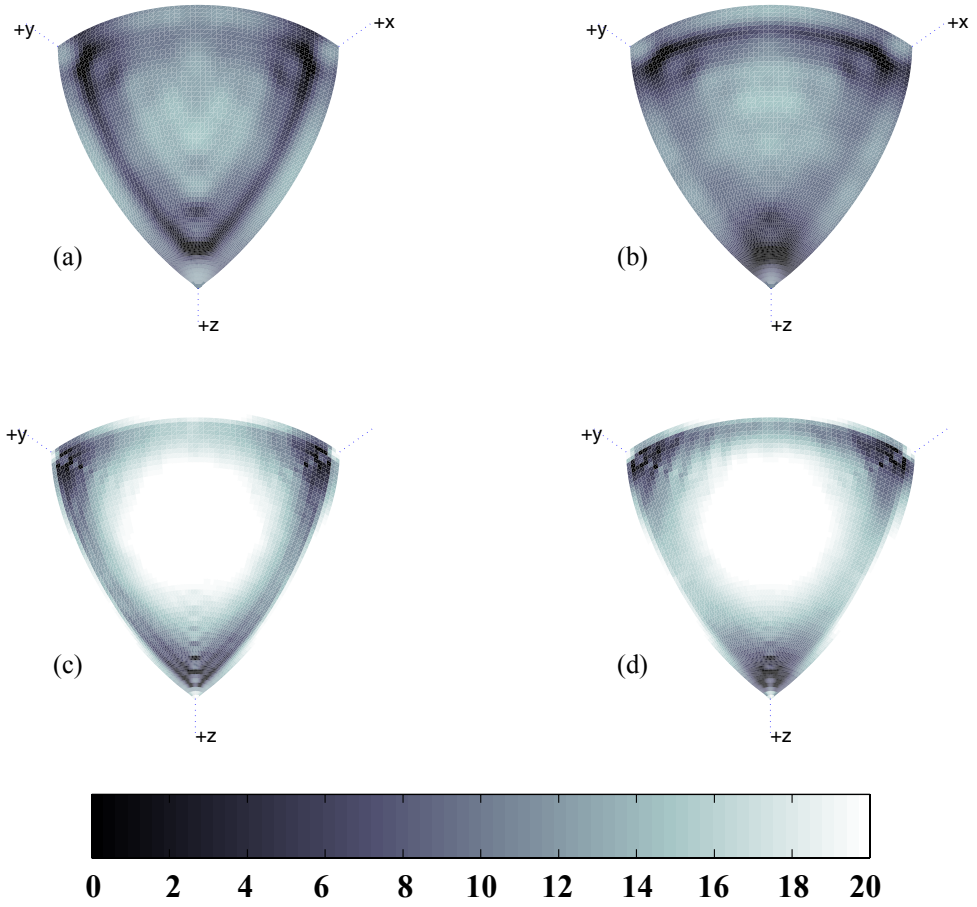

Fig. 7. Two-dimensional monostatic RCS plots of trihedral calculated with WIPL-D: (a) horizontal polarization at 1.5 GHz; (b) vertical polarization at 1.5 GHz; (c) horizontal polarization at 3.8 GHz; and (d) vertical polarization at 3.8 GHz.

3.2 Bistatic RCS

For the bistatic case, RCS is plotted versus arbitrary receive (observation) angles (ϕ_{obs}, θ_{obs}) in the positive *xyz* octant for three incident angles along the geometric half-plane of symmetry ($\phi = 45°$): (1) $\theta = 20.26°$, which is 15° above axis of symmetry (Figs. 8a,d); (2) $\theta = 35.26°$, which is the axis of symmetry (Figs. 8b,e); (c) $\theta = 50.26°$, which is 15° below axis of symmetry (Figs. 8c,f). On studying Fig. 8, one may infer that the bistatic RCS is significantly smaller than the monostatic RCS, that the patterns are symmetric about the geometric plane of symmetry, and that the polarizations yield different patterns. As θ_{obs} increases, the area of greatest RCS travels down the bisector of the curved triangular region and transforms from being vertically elongated to being horizontally elongated, regardless of the polarization. For θ_{obs} near the monostatic direction (35.26°), this area corresponds to the trihedral's effective aperture. Also, note the well defined bright spots outside the main

area of large RCS, which indicate that one can expect enhanced RCS from regions other than the main area. How the preceding results relate to the bistatic angle is left for a future discussion. To get a more concrete idea of the differences between polarizations, three cross-sectional curves are plotted for three incident directions and two receive angles ($\theta_{obs} = 35.26°$, $\phi_{obs} = 45°$) in Fig. 9.

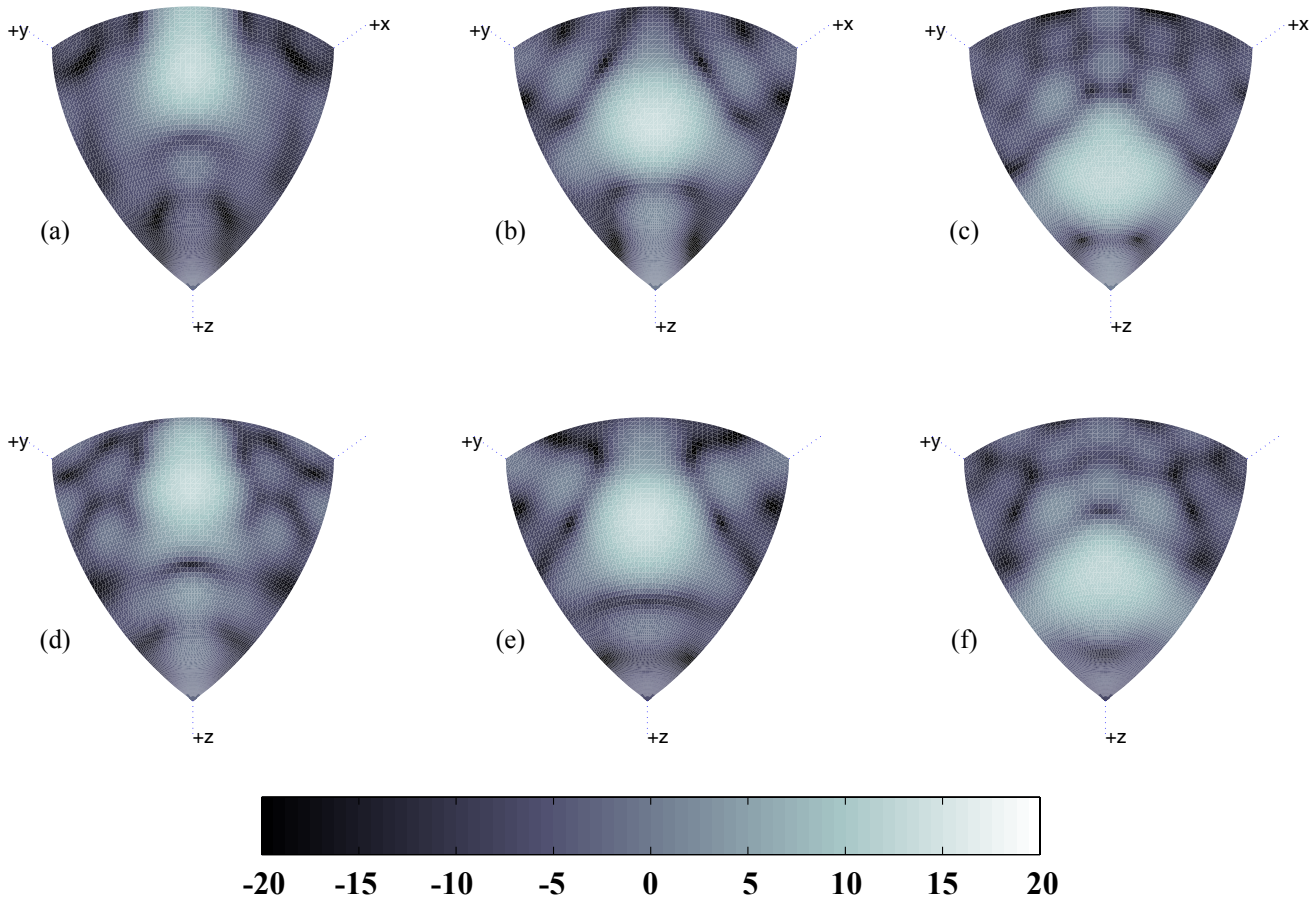

Fig. 8. Two-dimensional projections of bistatic RCSs of 1-m trihedral at 1.5 GHz for three incident directions (ϕ_{inc}, θ_{inc}) and both polarizations (horizontal – HPol, vertical – VPol): (a) HPol @ (45°,20.26°); (b) HPol @ (45°,35.26°); (c) HPol @ (45°,50.26°); (d) VPol @ (45°,20.26°); (e) VPol @ (45°,35.26°); (f) VPol @ (45°,50.26°).

4. Summary

This work represents initial WIPL-D(P) computational modeling of monostatic and bistatic scattering from the trihedral corner reflector as part of a larger application problem to characterize radar sea scatter. It is important to perform additional WIPL-D(P) calculations for several frequencies from 1-12 GHz so that: (1) it may be determined through convergence analyses whether WIPL-D(P) produces the best answer it can, given the limitations of the computer used to make the calculations; and (2) WIPL-D(P) predictions can be compared

to existing UWB radar data. In addition, the trihedral reflectors used for the collected radar data need to be measured in a compact range, and these range measurements should be compared to WIPL-D(P) predictions.

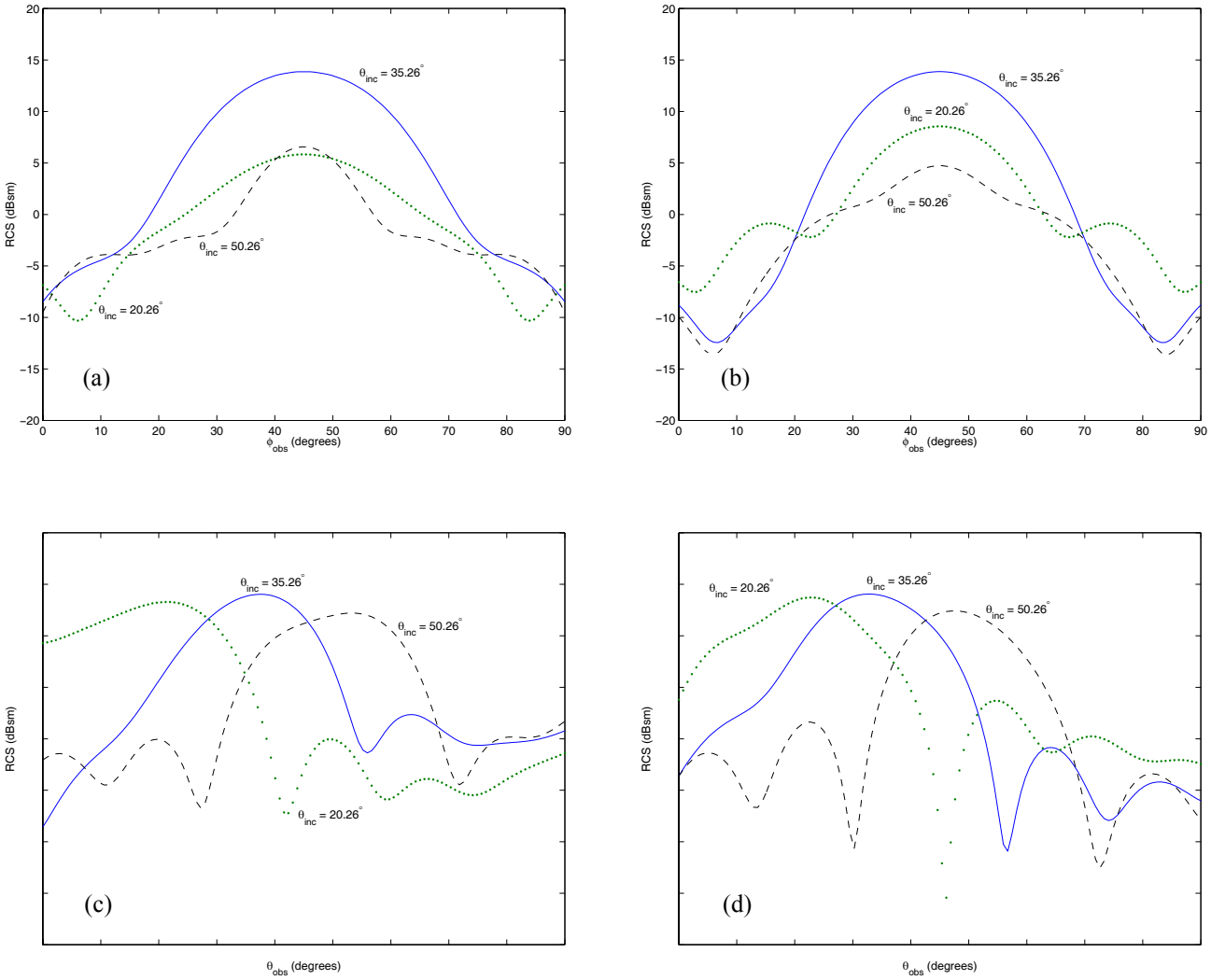

Fig. 9. Bistatic RCSs of 1-m trihedral at 1.5 GHz for incident directions [(45°,20.26°), (45°,35.26°), (45°,50.26°)]: (a) HPol @ $\theta_{obs} = 35.26°$; (b) VPol @ $\theta_{obs} = 35.26°$; (c) HPol @ $\phi_{obs} = 45°$; (d) VPol @ $\phi_{obs} = 45°$.

References

[1] B. Kolundzija, J.S. Ognjanovic, T.K. Sarkar, *WIPL-D: Electromagnetic Modeling of Composite Metallic and Dielectric Structures — Software and User's Manual* (Artech House, Norwood, 2000).

[2] L.B. Wetzel, "Sea Clutter," in *Radar Handbook*, 2nd edition, edited by M. Skolnik (McGraw-Hill, New York, 1990), Ch. 13.

[3] C.G. Bachman, *Radar Targets* (Lexington Books, Lexington, 1982), pp. 89–91.

[4] K. Sarabandi and T.-C. Chiu, "Optimum Corner Reflectors for Calibration of Imaging Radars," *IEEE Trans. Antennas Propagat.*, **44**(10), pp. 1348–1361, 1996.

[5] L. Peters, "Passive Bistatic Radar Enhancement Devices," *Proc. IEE*, **109**(15), pp. 1–10, 1962.

[6] P. Hansen, K. Scheff, E. Mokole, and E. Tomas, "Dual Frequency Measurements of Ocean Forward Scatter with an Ultrawideband Radar," Proceedings of the 2001 IEEE Radar Conference, Atlanta GA, pp. 376–381, May 1-3, 2001.

[7] R. Trebits, "Radar Cross Section," in *Radar Reflectivity Measurement: Techniques & Applications*, edited by N.C. Currie (Artech House, Norwood, 1989), Ch. 2, pp. 39–42.

[8] J. Baldauf, S.-W. Lee, L. Lin, S.-K. Jeng, S.M. Scarborough, and C.L. Yu, "High Frequency Scattering from Trihedral Corner Reflectors and Other Benchmark Targets: SBR Versus Experiment," *IEEE Trans. Antennas Propagat.*, **39**(9), pp. 1345–1351, 1991.

[9] R.C. Spencer, "Optical Theory of the Corner Reflector," MIT Radiation Laboratory Report 433, Cambridge MA, March 2, 1944.

